

A long-lived sharp disruption on the lower clouds of Venus

J. Peralta^{1*}, T. Navarro^{2,3,4}, C. W. Vun¹, A. Sánchez-Lavega⁵, K. McGouldrick⁶, T. Horinouchi⁷, T. Imamura⁸, R. Hueso⁵, J. P. Boyd⁹, G. Schubert², T. Kouyama¹⁰, T. Satoh¹, N. Iwagami¹¹, E. F. Young¹², M. A. Bullock¹², P. Machado¹³, Y. J. Lee¹⁴, S.S. Limaye¹⁵, M. Nakamura¹, S. Tellmann¹⁶, A. Wesley¹⁷ and P. Miles¹⁸

¹Institute of Space and Astronautical Science, JAXA, Sagami-hara, Japan.

²Department of Earth, Planetary, and Space Sciences, University of California, Los Angeles, CA, USA.

³McGill Space Institute, McGill University, Montréal, QC, Canada.

⁴Department of Earth and Planetary Sciences, McGill University, Montréal, QC, Canada.

⁵(5) Escuela de Ingeniería de Bilbao, UPV/EHU, Bilbao, Spain.

⁶Laboratory for Atmospheric and Space Physics, Univ. of Colorado Boulder, Boulder, CO, USA.

⁷Faculty of Environmental Earth Science, Hokkaido University, Hokkaido, Japan.

⁸Graduate School of Frontier Sciences, The University of Tokyo, Tokyo, Japan.

⁹CLaSP Department, University of Michigan College of Engineering, Ann Arbor, USA.

¹⁰Artificial Intelligence Research Center, National Institute of Advanced Industrial Science and

Technology, Japan.

¹¹Tokyo 156-0044, Japan.

¹²Southwest Research Institute, Boulder, CO 80302, USA.

¹³Institute of Astrophysics and Space Sciences, Portugal.

¹⁴Technische Universität Berlin, Berlin, Germany.

¹⁵Space Science and Engineering Center, University of Wisconsin, Madison, WI, USA.

¹⁶Abteilung Planetenforschung, Rheinisches Institut für Umweltforschung, Universität zu Köln, Cologne,

Germany.

¹⁷Astronomical Society of Australia, Murrumbateman, New South Wales, Australia.

¹⁸Gemeye Observatory, Rubyvale, Queensland, Australia.

Key Points:

- Discovery of an equatorial sharp cloud discontinuity at the middle and lower clouds of Venus, where no planetary wave had been found before.
- This disruption propagates to the West faster than the winds, keeps coherent for weeks and alters clouds' properties and aerosols.
- Past observations confirm its existence since 1983. Numerical simulations suggest a physical origin as a nonlinear Kelvin wave.

This is the author manuscript accepted for publication and has undergone full peer review but has not been through the copyediting, typesetting, pagination and proofreading process, which may lead to differences between this version and the Version of Record. Please cite this article as doi: [10.1029/2020GL087221](https://doi.org/10.1029/2020GL087221)

*Currently unemployed, Algeciras, Spain.

Corresponding author: Javier Peralta, javier.peralta@ac.jaxa.jp

Abstract

Planetary-scale waves are thought to play a role in powering the yet-unexplained atmospheric superrotation of Venus. Puzzlingly, while Kelvin, Rossby and stationary waves manifest at the upper clouds (65–70 km), no planetary-scale waves or stationary patterns have been reported in the intervening level of the lower clouds (48–55 km), although the latter are probably Lee waves. Using observations by the Akatsuki orbiter and ground-based telescopes, we show that the lower clouds follow a regular cycle punctuated between 30°N–40°S by a sharp discontinuity or disruption with potential implications to Venus’s general circulation and thermal structure. This disruption exhibits a westward rotation period of ~ 4.9 days faster than winds at this level (~ 6 -day period), alters clouds’ properties and aerosols, and remains coherent during weeks. Past observations reveal its recurrent nature since at least 1983, and numerical simulations show that a nonlinear Kelvin wave reproduces many of its properties.

Plain Language Summary

One of the biggest mysteries of Venus is its atmospheric superrotation that allows the atmosphere to rotate 60 times faster than the solid planet. Atmospheric waves are among one of the possible mechanisms thought to feed this superrotation by pushing energy to different locations of the atmosphere. In fact, the upper clouds of Venus located at 65–70 km exhibit varied giant waves, like the so-called Y-feature or the more recently-discovered bow-shape wave that keeps “stationary” over Aphrodite mountains. In contrast, these planetary-scale waves are missing at the deeper lower clouds (48–55 km). This is especially puzzling in the case of the stationary waves since the lower clouds are located between the upper clouds and the surface, where they are thought to be generated. Thanks to the high-quality observations of Venus from JAXA’s space mission Akatsuki and NASA’s IRTF telescope, we discovered at the lower clouds an intriguing sharp discontinuity that propagates to the west faster than the winds while altering the clouds’ properties and suffering little distortions during weeks. A re-analysis of past observations revealed that this is a recurrent phenomenon that has gone unnoticed since at least the year 1983. Numerical simulations evidence that an atmospheric wave generated below the clouds and probably pumping energy to the upper clouds can explain many of its properties.

1 Introduction.

The atmosphere of Venus is dominated by superrotating winds that at the cloud layers (~ 48 –70 km) (Titov et al., 2018) exhibit speeds 60 times faster than the planet (Sánchez-Lavega et al., 2017). The clouds of Venus are mostly composed of H_2SO_4 - H_2O droplets and are stratified into three layers (Titov et al., 2018). In the upper clouds (56.5–70 km above the surface), absorbers of known and unknown composition are responsible for the dark markings observed in ultraviolet images and for most of the absorption of the solar energy not reflected by the clouds (Titov et al., 2018). The middle and lower clouds (hereafter, simply named *deeper clouds*) are within 47.5–56.5 km and importantly contribute to the greenhouse effect and the radiative energy balance. These clouds exhibit variable cloud optical thickness (Titov et al., 2018; McGouldrick et al., 2012; Peralta, Iwagami, et al., 2019) in a region where the lapse rate is close to adiabatic and convection dominates vertical transport, as shown by observations (Yakovlev et al., 1991; Hinson & Jenkins, 1995; Tellmann et al., 2009; Ando et al., 2020) and modelling (Imamura et al., 2014; Lefèvre et al., 2018). The middle clouds (50.5–56.5 km) are observed on the dayside at visible and near-infrared (900–1000 nm) wavelengths (Titov et al., 2018; Peralta, Iwagami, et al., 2019), while the lower clouds (47.5–50.5 km) are observed on the nightside using spectral windows at 1.74, 2.26 and 2.32 μm (McGouldrick et al., 2012; Titov et al., 2018; Limaye et al., 2018). Clouds’ morphology and motions are different

85 at each of these layers (Sánchez-Lavega et al., 2017; Peralta, Iwagami, et al., 2019; Titov
86 et al., 2018; Limaye et al., 2018; Peralta, Sánchez-Lavega, et al., 2019; Horinouchi et al.,
87 2017).

88 It has long been proposed that planetary-scale waves could play a role in power-
89 ing the superrotation (Sánchez-Lavega et al., 2017). Some of them manifest visually at
90 the upper clouds (65–70 km), like the Y-feature (Peralta et al., 2015) and the station-
91 ary bow-shaped wave (Fukuhara et al., 2017). Some others manifest in the wind field
92 like thermal tides (Kouyama et al., 2019), Kelvin and Rossby waves (Imai et al., 2019)
93 and stationary features (Peralta et al., 2017). However, no planetary-scale waves or sta-
94 tionary patterns have been reported in the intervening level of the lower clouds (Peralta
95 et al., 2008, 2017; Peralta, Sánchez-Lavega, et al., 2019; Peralta, Iwagami, et al., 2019)
96 (48–55 km), even though stationary waves are probably generated at the surface (Navarro
97 et al., 2018).

98 2 Methods.

99 The nightside lower clouds of Venus were studied using 1,519 images acquired at
100 1.735, 2.26 and 2.32 μm during April–November 2016 by the IR2 camera (Satoh et al.,
101 2017) onboard the Akatsuki orbiter (Nakamura et al., 2016), giving preference to 2.26-
102 μm images (238 useful images), which were less affected by light contamination from the
103 saturated dayside (Satoh et al., 2017). The periods January–February 2017, November–
104 December 2018 and January 2019 were studied with 78 K_{cont} (2.32- μm) images from the
105 instruments SpeX and iSHELL (J. T. Rayner et al., 2003; J. Rayner et al., 2012) at NASA’s
106 Infrared Telescope Facility (IRTF). We also reanalyzed 376 images from the Visible and
107 Infrared Thermal Imaging Spectrometer (VIRTIS) covering April 2006 to October 2008
108 during the Venus Express (VEx) mission (Drossart et al., 2007). The dayside middle clouds
109 were inspected from December 2015 to December 2016 using 984 Akatsuki/IR1 900-nm
110 images (Iwagami et al., 2018), although October 2016 was covered with 29 1- μm images
111 from a 0.5-m ground-based telescope since the phase angle from Akatsuki was large. The
112 spatial resolution of Akatsuki images ranges 74–0.2 km/pixel depending on the distance
113 between the spacecraft and the planet (Nakamura et al., 2016), while for ground-based
114 observations it varies from 29–65 km (IRTF) to 400 km (0.5-m telescope) (Sánchez-Lavega
115 et al., 2016). A summary of the imagery dataset is shown in Table S1.

116 2.1 Image Processing.

117 Akatsuki IR1 and IR2 cameras have CSD/CCD and PtSi-CSD/CCD detectors re-
118 spectively, with dimensions 1024×1024 and their images present some specific problems
119 (Satoh et al., 2017; Iwagami et al., 2018). IR2 images sensing Venus’s nightside at 1.74,
120 2.26 and 2.32 μm in the calibration version of this work (v20180201) present a problem
121 of light contamination with halation rings and a cross pattern that extends horizontally
122 and vertically around the saturated dayside of the planet, spreading with multiple re-
123 flections along the PtSi detector (Satoh et al., 2017). IR2 images taken with the 2.26-
124 μm filter were chosen for the characterization of clouds’ morphology and motions, since
125 the contamination is sufficiently reduced in them. We reduced the light contamination
126 with an image processing procedure consisting on an adjustment of the brightness/contrast,
127 followed by convolution with unsharp-mask image filter, and finally adaptive histogram
128 equalization (Peralta et al., 2018; Peralta, Sánchez-Lavega, et al., 2019). This procedure
129 is not totally efficient, and the effect of light contamination is yet apparent in some of
130 the Figures in this work (Figs. 1). The images of the nightside acquired with the guide
131 camera of IRTF/SpeX (J. T. Rayner et al., 2003) and a K_{cont} filter were subtracted with
132 sky images and flat-fielded corrected, though they lacked absolute calibration. Light con-
133 tamination from the saturated dayside was efficiently reduced by subtracting these im-

134 ages with other acquired with a B γ filter (2.18 μm). The processing technique afterwards
135 was like the one applied on IR2 images, skipping the adaptive histogram equalization.

136 IR1 900-nm dayside images suffered from the added effect of smear noise, a bright-
137 ness mismatch among the four quadrants of the camera sensor and a very small signal-
138 to-noise (S/N) ratio (Iwagami et al., 2018). Except for the latter, these effects are rea-
139 sonably well corrected in the calibration version v20180201. To increase the S/N of the
140 IR1 images, we applied a photometric Minnaert correction (Peralta, Iwagami, et al., 2019)
141 followed by brightness/contrast enhancement, smoothing with a radius of 2-3 pixels and
142 a later unsharp-mask. This procedure successfully enhances the cloud features, especially
143 in IR1 images with smaller phase angle (and better S/N), although it also enhances bright-
144 ness mismatch among the quadrants of the sensor (see Figs. 1B, 2A and 2C). The im-
145 ages from small telescopes were acquired with a 508-mm Newtonian telescope, a FLIR
146 GS3-U3-32S4M-C camera and a Thorlabs FELH1000 1- μm long-pass filter. These ground-
147 based images covered 18 days from 9 to 30 of October 2016, with a solar elongation of
148 35 $^\circ$, a mean diameter of about 13 arcsecs, and an 80% of illuminated fraction. As with
149 the IR1/900-nm images, we applied a Minnaert photometric correction followed by unsharp-
150 mask (see examples in Figure S4).

151 2.2 Navigation of images.

152 Small uncertainties are known to affect the pointing of Akatsuki cameras, inhibit-
153 ing high accuracy in the navigation of the Venus images (Ogohara et al., 2017). The im-
154 age navigation was corrected using an ellipse fitting procedure where an automatic de-
155 termination of the planetary limb pixels corrects the pointing (Ogohara et al., 2017; Satoh
156 et al., 2017; Horinouchi et al., 2017). This automated method was used for the IR1 im-
157 ages but discarded in the case of IR2 and SpeX since light contamination and frequent
158 darkening of the clouds' opacity make difficult the automatic identification of the plan-
159 etary limb. For these images, we used a software tool (Peralta et al., 2018) which im-
160 proves the visualization of the limb through image processing and allows to perform a
161 visual adjustment of the position, size and orientation of the planet's grid. In the case
162 of the IR2 images, the orientation of the navigation grid is kept unmodified, while the
163 position of the grid was adjusted with a precision of 1/10 of a pixel. Images from SpeX,
164 iSHELL and small telescope were firstly navigated using NASA's SPICE kernels, and
165 both position and orientation of the grid were adjusted.

166 2.3 Calculation of cloud properties using VEx/VIRTIS images.

167 Due to the problem of light contamination in the images of Akatsuki/IR2, we con-
168 sidered only VEx/VIRTIS images (see Table S1) to study the effect of the cloud discon-
169 tinuity on the optical depth and size parameter of the nightside lower clouds (see, Figs. 3B
170 and 3C). Prior to calculating the optical thickness and size parameter, we performed a
171 correction of the limb darkening in images at 1.74 and 2.30 μm , following the formula
172 given by Wilson et al. (2008):

$$173 \quad I_{1.74\mu\text{m}} = \frac{I'_{1.74\mu\text{m}}}{0.316 + 0.685 \cdot \cos EA} \quad (1)$$

$$174 \quad I_{2.30\mu\text{m}} = \frac{I'_{2.30\mu\text{m}}}{0.232 + 0.768 \cdot \cos EA} \quad (2)$$

175 where $I'_{1.74\mu\text{m}}$ and $I'_{2.30\mu\text{m}}$ are the observed radiances and EA is the emission angle.

176 The optical depth τ was calculated using VIRTIS images at 1.74 μm as $\tau = \log(I_{1.74\mu\text{m}}^{max}/I_{1.74\mu\text{m}})$,
177 where $I_{1.74\mu\text{m}}^{max}$ and $I_{1.74\mu\text{m}}$ are, respectively, the maximum value of radiance and the ra-
178 diance at every pixel in the image. The size parameter m was calculated following the
179 method of Carlson et al. (1993) using the formula adapted for VIRTIS by Wilson et al.

180 (2008): $m = (I_{1.74\mu\text{m}}) / (I_{2.30\mu\text{m}})^{0.53}$, where $I_{1.74\mu\text{m}}$ and $I_{2.30\mu\text{m}}$ are the calibrated ra-
 181 diances of the Venus images at 1.74 and 2.30 μm .

182 2.4 Simulations with the IPSL Venus GCM.

183 The IPSL (Institut Pierre-Simon Laplace) GCM (General Circulation Model) is
 184 a full-physics model that includes, among other things, radiative transfer for solar and
 185 thermal radiations, a boundary layer scheme, topography, hybrid vertical coordinates,
 186 and a temperature-dependent heat capacity (Lebonnois et al., 2010, 2016; Garate-Lopez
 187 & Lebonnois, 2018). The resolution used for the longitude-latitude grid is 96×96 , and
 188 the configuration is the same as in Garate-Lopez and Lebonnois (2018), who arbitrar-
 189 ily increased solar heating rates of the poorly constrained properties of the lower haze
 190 below the cloud base in order to match observed temperatures. Superrotation is fully
 191 developed in numerical simulations with this model after 300 Venus solar days of sim-
 192 ulation.

193 The GCM predicts zonal speeds of 45 m s^{-1} at the bottom of the cloud deck (48
 194 km) (see Fig. 4D), slower than the 60 m s^{-1} from in-situ measurements by Pioneer Venus
 195 descent probes (Counselman et al., 1980). To correct this, we added an extra term in
 196 the dynamic core of the model to the equation of zonal momentum for latitudes equa-
 197 torward of 50° :

$$198 \quad \frac{du}{dt} = \dots + (u_f - u) \cdot k(P) \quad (3)$$

199 with u being the zonal wind, u_f the forced zonal wind profile, and $k(P)$ a pressure-dependent
 200 coefficient:

$$201 \quad k(P) = 10^{-6} \cdot \frac{1 + \tanh(\log(P/10^5))}{2} \quad (4)$$

202 The forced wind zonal profile u_f is constructed from the temporally and zonally aver-
 203 aged zonal winds from the standard simulation of Garate-Lopez and Lebonnois (2018),
 204 increased by 30%. This relaxed simulation starts from the initial state of fully developed
 205 superrotation from the standard simulation, and it converges to increased steady aver-
 206 aged zonal winds in less than a Venus day.

207 3 Results.

208 To study the global opacity and morphology of the deeper clouds over several rev-
 209 olutions of the mean flow (~ 5 -6 day period; see Horinouchi et al., 2017; Peralta et al.,
 210 2018; Peralta, Iwagami, et al., 2019), we constructed time composites combining equirect-
 211 angular projections of the images shifted according to the zonal background wind (see
 212 Figure 1; animations of panels 1C and 1E can be found in Movie S1). At low latitudes,
 213 the nightside lower clouds show a variable dark band (higher opacity) (Crisp et al., 1991),
 214 while bright (lower opacity) bands dominate at mid-latitudes. The lower clouds drift to
 215 the west following a ~ 5 -6-day cycle. The equatorial band dominated by dark feature-
 216 less clouds (longitude drift 40° - 100° in Fig. 1A or 240° - 300° in Fig. 1B) is observed to
 217 become narrower as mid-latitude bands gradually invade lower latitudes. Simultaneously,
 218 it exhibits bright swirls and other patterns reminiscent of von Kármán vortex streets (Fig. 1A)
 219 and the borders with the mid-latitude bands adopt a wavy shape (wavelengths ranging
 220 4,000-6,000 km) with mesoscale billows and vortices (Peralta, Sánchez-Lavega, et al.,
 221 2019; Horinouchi et al., 2017; Satoh et al., 2017). The cycle ends when the dark band
 222 develops brighter clouds that are abruptly interrupted by a sharp discontinuity or dis-
 223 ruption. During August 2016 (Fig. 1A), an equatorial jet was observed (Horinouchi et
 224 al., 2017) $\sim 150^\circ$ - 200° west from the disruption. In October 2016 (Fig. 1C), the discon-
 225 tinuity became weaker, the equatorial jet seemed missing and the mid-latitude bands merged
 226 at the equator forming a bright trough (Peralta, Sánchez-Lavega, et al., 2019). An ex-
 227 amination of 85 radio-occultation profiles within 30°N - 30°S obtained during 2006-2016

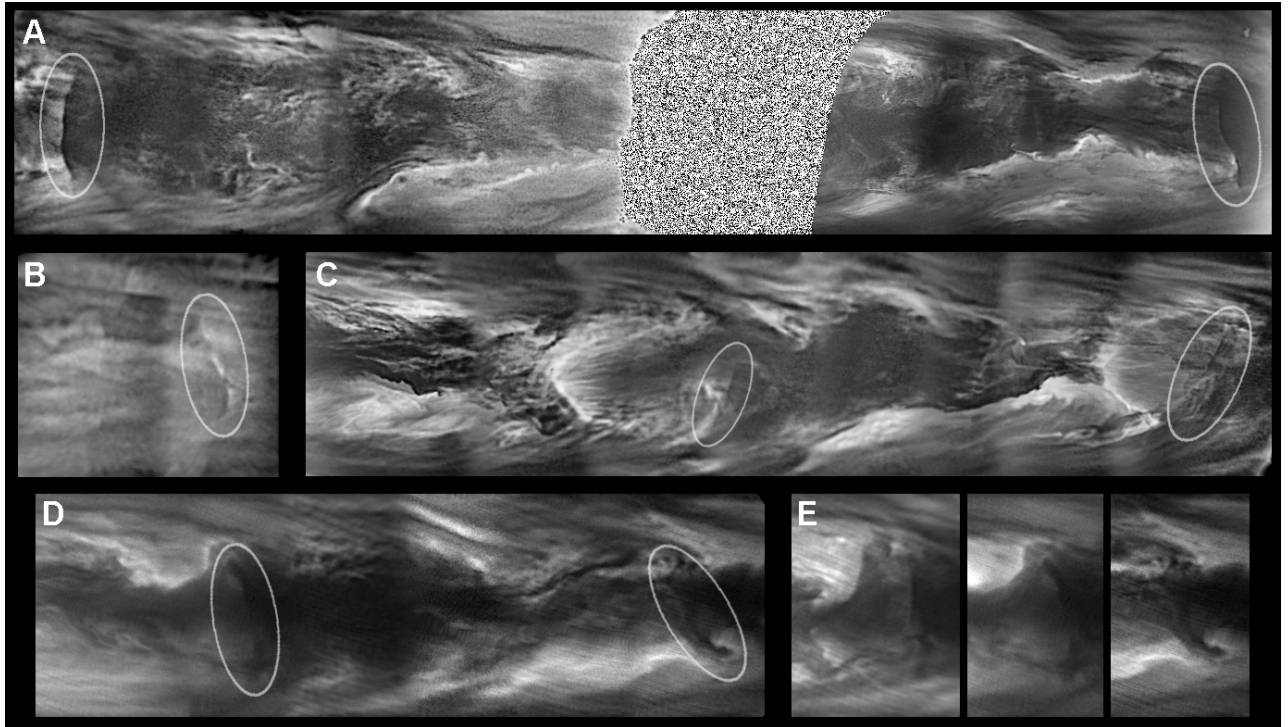


Figure 1. The cycle of the deeper clouds of Venus. Time composites of the deeper clouds displayed with overlapped equirectangular projections (60°N – 60°S and 0.5° per pixel) placed from left to right with increasing dates: (A) 2016 August 18–22 and 25–27 (IR2- $2.26\ \mu\text{m}$), (B) 2016 May 3–4 (IR1- $900\ \text{nm}$), (C) 2016 October 10–17 (IR2- $2.26\ \mu\text{m}$) and (D) 2018 December 1–6 (SpeX- $2.3\ \mu\text{m}$). Panel (E) exhibits the evolution of a case of disruption in November 27 and December 2 and 6 of 2018 (SpeX- $2.3\ \mu\text{m}$). All images display the nightside of Venus except (B).

228 by VEx and Akatsuki reveals that this cycle implies night-time variations of 2–6% in at-
 229 mospheric temperature, pressure and molecular density (see Fig. S1).

230 The sharp cloud discontinuity is a recurrent phenomenon at both lower and mid-
 231 dle clouds (Figs. 1B and 2A; see Movie S2), although it is apparently missing in obser-
 232 vations of the upper clouds (Yamazaki et al., 2018; Satoh et al., 2017) (Fig. 2C). The
 233 discontinuity is sometimes followed by undulations with wavelengths of $65\pm 14\ \text{km}$ (Fig. 2B),
 234 and can also extend thousands of kilometers westward from their northernmost end giv-
 235 ing birth to sharp dark stripes (Figs. 1A and 1D) previously reported (Peralta, Sánchez-
 236 Lavega, et al., 2019). Table S1 contains a summary of all the events of cloud disruptions.
 237 During 2016, 35 events were identified in the Akatsuki observations (Figs. S2–S3), and
 238 probably twice more in observations with small telescopes (Figs. S4A–B). IRTF/SpeX
 239 observations between 2017 and 2019 revealed 7 events (Figs. S4C–D). A reanalysis of pub-
 240 lished ground-based observations (Allen & Crawford, 1984; Crisp et al., 1991; Bailey, 2006;
 241 Peralta et al., 2018) shows that the disruption was present on Venus’s lower clouds in
 242 September 1983, January–February 1990, December 2005, July 2012 (Fig. 2D), and at
 243 least 12 times during 2006–2008 in VEx/VIRTIS images (see Figs. S4E–H).

244 Figure 3A displays the rotation period, orientation and latitudinal extent of the
 245 disruption from 2016 until early 2019. The disruption appears within latitudes 30°N –
 246 40°S , it can have a length that varies from 800 ± 50 to $7,600\pm 200\ \text{km}$ and has a mean width

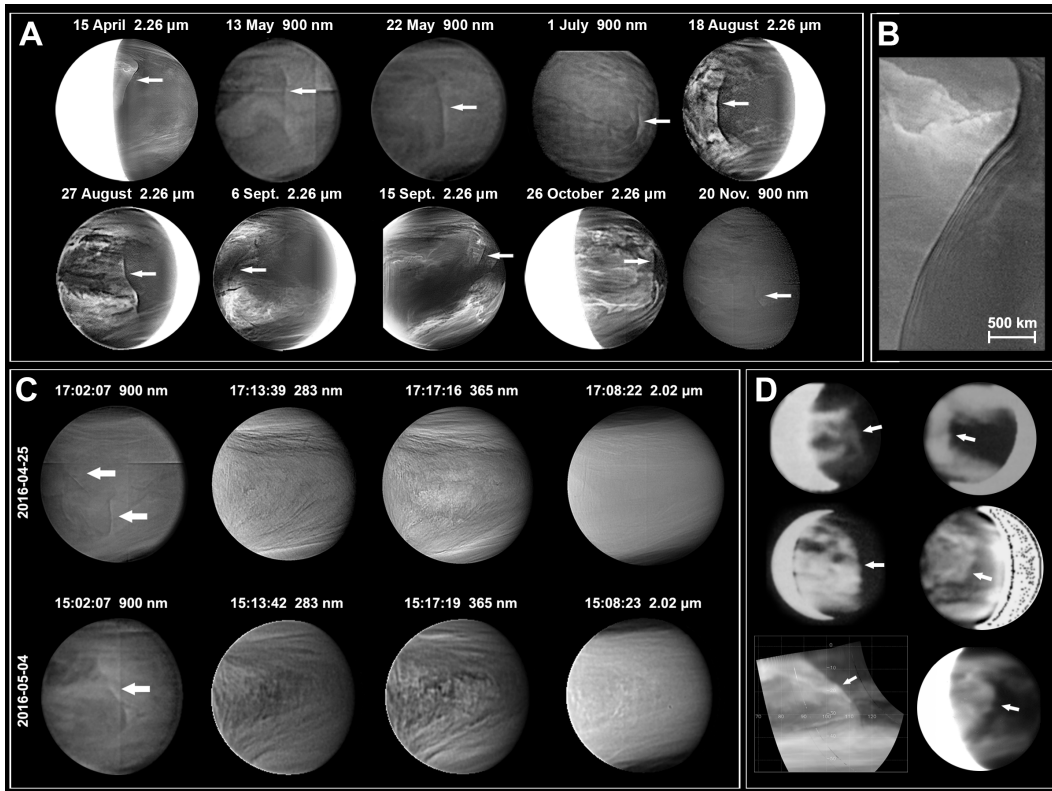


Figure 2. Morphology, vertical extension and recurrence of Venus's disruption. (A) morphological changes of the cloud discontinuity during 2016 on images from IR1/900-nm (dayside) and IR2/2.26- μm (nightside). Full set in Figs. S2–S3; (B) example of undulations behind a discontinuity in 15 April 2016; (C) discontinuities apparent on the middle clouds (IR1) but not at the upper clouds sensed with ultraviolet (UVI) and 2.02- μm images (IR2); (D) past events of disruption (left-to-right, top-to-bottom): September 1983 (Allen & Crawford, 1984), January/February 1990 (Crisp et al., 1991), December 2005 (Bailey, 2006), September 2006 (VEx/VIRTIS) and July 2012 (Peralta et al., 2018). All images were high-pass filtered (see subsection 2.1). Disruptions are marked with arrows.

247 of 280 ± 140 km (cross-to-along ratio $\sim 1:13$). Its mean orientation relative to the equa-
248 torial plane is $85^\circ \pm 18^\circ$ but ranges from 35° to 132° . In rare cases, the cloud disconti-
249 nuity is seen split into two or three elements with different orientations (Fig. 2C). Dur-
250 ing August 2016, the disruption kept approximately coherent for ~ 20 days. However,
251 in general, the disruption suffers distinguishable changes after one revolution (Figs. 2A
252 and S2), and its morphology and hemispherical symmetry/asymmetry seem unrelated
253 to surface elevations (see Fig. S5). The disruption propagates to the west with a mean
254 zonal speed of -91 ± 9 m s $^{-1}$ —similar to the equatorial jet when this is present (Horinouchi
255 et al., 2017)—and faster than the background winds within 30°N – 40°S (see Fig. 1E), which
256 are -68 ± 9 m s $^{-1}$ at the lower clouds (48–55 km) (Peralta et al., 2018) and -74 ± 9
257 m s $^{-1}$ at the middle clouds (~ 55 – 65 km) (Sánchez-Lavega et al., 2017; Peralta, Iwagami,
258 et al., 2019). Considering the overall data, the rotation period of this disruption is 4.9 ± 0.5
259 days (Fig. 3A). Separate analyses of data for the middle and lower clouds yield periods
260 of 4.7 ± 0.4 and 5.0 ± 0.5 days, respectively. The zonal drift of the disruption experienced
261 larger variations in September (10 m s $^{-1}$) and November 2016 (~ 30 m s $^{-1}$). Observa-
262 tions during November 2018 and January 2019 suggest that the drift of this feature in-
263 creased by 40 m s $^{-1}$ during its propagation on the dayside (Figs. 3A and 1E).

264 VEx/VIRTIS images were used to study other effects of the disruption. On the night-
265 side, the passage of the discontinuity implies radiance decreases of $75 \pm 7\%$, $88 \pm 7\%$ and
266 $88 \pm 6\%$ at 1.74 , 2.26 and 2.32 μm respectively (see Table S2), while on dayside IR1/900-
267 nm images it implies albedo changes of only 1%–4% (Peralta, Iwagami, et al., 2019). The
268 optical thickness (Fig. 3B) is observed to increase one order of magnitude west-to-east
269 across the disruption, while its effect over the size parameter (regarded to be a proxy for
270 particle size; see Carlson et al., 1993) is more variable although the west-side of the dis-
271 ruption is frequently linked to more abundance of smaller particles (Fig. 3C). This sce-
272 nario seems consistent with downwelling and clouds’ evaporation (McGouldrick et al.,
273 2012) (hence, lower optical thickness) west of the disruption, and upwelling accompa-
274 nished by formation of clouds (larger optical thickness) on its east-side. This upwelling com-
275 bined with the increased H $_2$ SO $_4$ vapor pressure and the larger nucleation rates expected
276 for the high H $_2$ SO $_4$ concentrations of the clouds (Sihto et al., 2009; Titov et al., 2018)
277 can help the cloud condensation nuclei (CNN) of submicron size to overcome the Kelvin
278 barrier (i.e. greater saturation pressure over smaller particles) and grow to small droplets
279 with radii of ~ 1 μm (Imamura & Hashimoto, 2001), probably explaining the abundance
280 of smaller particles observed in Fig. 3C.

281 Considering its morphology, long-term coherence and its westward drift faster than
282 the mean flow, the disruption might be the manifestation of a weakly-dispersive Kelvin
283 front (a nonlinear Kelvin wave). Kelvin fronts can be often undular like observed in Fig-
284 ure 2B, exhibiting gravity wave resonances excited behind the leading edge and prop-
285 agating with the same phase speed (Fedorov & Melville, 2000). Day-night differences in
286 stability and wind shear can change the intrinsic phase speed of a Kelvin wave (Peralta
287 et al., 2015) and explain its faster propagation during its dayside passage (Fig. 3A). Sim-
288 ulations of the deeper clouds with the IPSL Venus GCM (Garate-Lopez & Lebonnois,
289 2018) (which does not incorporate interactions between circulation and clouds’ processes)
290 show that Kelvin fronts arise between 45–68 km under realistic atmospheric conditions
291 (Scarica et al., 2019), they affect zonal and meridional speeds and—more weakly—tem-
292 peratures (Fig. 4), and they barely interact with mountain waves (Fig. S6). At 55 km,
293 convection dominates vertical motions, explaining why the Kelvin wave is not apparent
294 in Fig. 4G. The sharpest gradient/discontinuity in zonal winds is found at 57 km (Fig. 4B)
295 and periodograms at different altitudes (Fig. 4H) evidence that the wave is trapped within
296 the deeper clouds with a westward rotation period of ~ 5.7 days, slower than the 4.9-day
297 average from observations but between minimum/maximum periods reported. The ro-
298 tation period is sensitive to the zonal winds below the clouds, being closer to observa-
299 tions when setting the relaxed profile of winds in the GCM (see subsection 2.4).

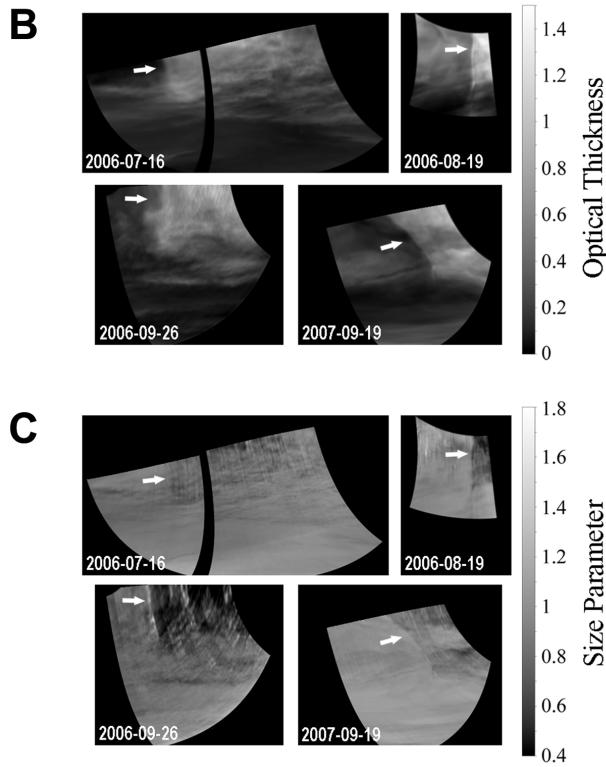
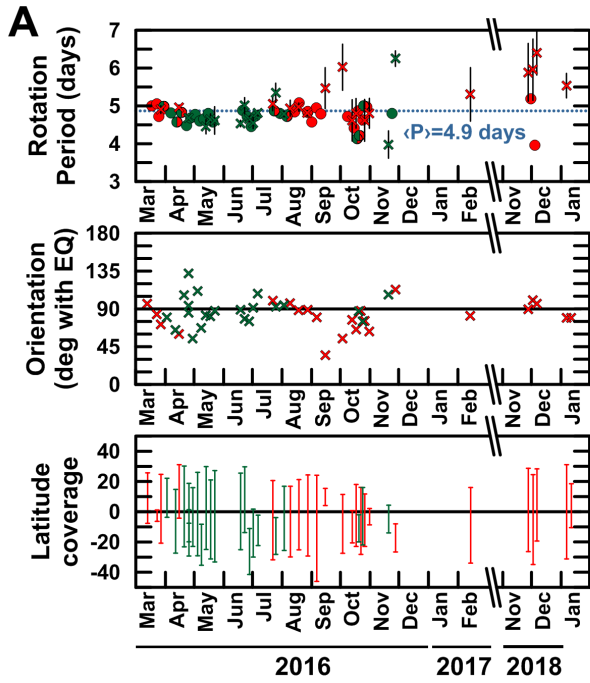


Figure 3. Properties of the cloud disruption. (A) Rotation period (mean period with blue-dotted line), orientation and latitude coverage of the disruption along 20162019. The periods were measured from the position of the disruption at the equator in images separated by hours (crosses) and several days (dots). When the disruption did not intersect the equator, we considered its longitude closest to the equator. Day/nightside data are shown in green/red, respectively. (B)–(C) Effect of the disruptions over the optical thickness ($1.74 \mu\text{m}$) and size parameter (1.74 and $2.32 \mu\text{m}$) in equirectangular projections (0° – 60°S , $0.2^\circ \cdot \text{pix}^{-1}$) of VEx/VIRTIS images (see subsection 2.3).

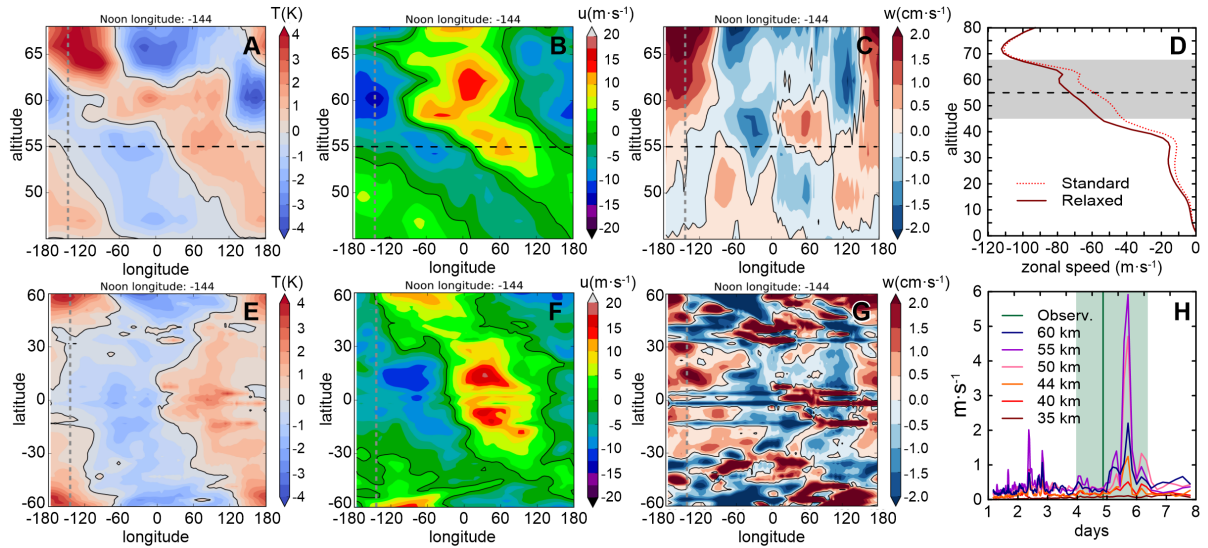


Figure 4. Kelvin wave according to a Venus GCM. Wave disturbances on temperatures and zonal and vertical speeds are shown as vertical cross-sections within 45–68 km (A–C) and horizontal ones at 55 km (E–G). (D) shows the standard and relaxed profiles of zonal winds (see subsection 2.4), with the grey-shaded area marking the altitudes in (A–C). (H) displays periodograms of the zonal speeds at several altitudes, with the green line/shaded-area standing for the averaged and minimum/maximum rotation periods from observations of the disruption. Noon longitude and 55-km altitude are shown with grey and black dashed lines, respectively.

4 Conclusions.

While stationary waves seem abundant at the upper clouds of Venus (56.5–70 km), the middle and lower clouds (47.5–56.5 km) do not exhibit stationary waves but a dark band with cyclical behavior and a sharp cloud discontinuity at equatorial latitudes with long-term coherence and apparently unrelated to the Venesian topography. The absence of observable signatures of this discontinuity at the upper clouds, where waves exhibit an evanescent nature (Imai et al., 2019) contrasts with its quasi-permanent nature at the middle and lower clouds.

Simulations with the IPSL Venus GCM show that a nonlinear Kelvin wave generated below the clouds (Yamamoto & Tanaka, 1997) reasonably reproduces this disruption and many of its observed properties (Fig. 4). Bore waves generated by katabatic fronts at the surface (Magdalena et al., 2006) or at higher altitudes by convective entrainment (Haghi et al., 2017) are alternative explanations to be explored by future studies, which might elucidate the role of this feature in the transport of atmospheric momentum and aerosols in the clouds of Venus.

Acknowledgments

The Akatsuki dataset is available at JAXA’s public repository (<http://darts.isas.jaxa.jp/planet/project/akatsuki/>). IRTF/SpeX images can be requested on reasonable request and will become available at the NASA/IPAC Infrared Science Archive (<https://irsa.ipac.caltech.edu/applications/irtf/>). VEx dataset is available at ESA’s public repository (<ftp://psa.esac.esa.int/pub/mirror/VENUS-EXPRESS/>).

J.P. acknowledges JAXA’s International Top Young Fellowship. T.N. and G.S. thank NASA’s Grant NNX16AC84G. A.S.-L. and R.H. were supported by Spanish project AYA2015-

65041-P (MINECO/FEDER, UE) and Grupos Gobierno Vasco IT-765-13. N.I. thanks
partial support by JSPS KAKENHI Grant JP16H02225. Y.J.L. received funding from
EU H2020 MSCA-IF No.841432. P.M. acknowledges FCT's project P-TUGA PTDC/FIS-
AST/29942/2017. S.S.L. thanks NASA's Grant NNX16AC79G. All authors acknowledge
the hard work done by the Akatsuki team. Sincere thanks to James O'Donoghue for proof-
reading this paper.

References

- Allen, D. A., & Crawford, J. W. (1984, January). Cloud structure on the dark side
of Venus. *Nature*, *307*, 222-224.
- Ando, H., Imamura, T., Tellmann, S., Pätzold, M., Häusler, B., Sugimoto, N., ...
Antonita, M. (2020, February). Thermal structure of the Venusian atmosphere
from the sub-cloud region to the mesosphere as observed by radio occultation.
Scientific Reports, *10*, 3448. doi: 10.1038/s41598-020-59278-8
- Bailey, J. (2006). Probing the Atmosphere of Venus using Infrared Spectroscopy. In
Proceedings of the 6th Australian space science conference (p. 23).
- Carlson, R. W., Kamp, L. W., Baines, K. H., Pollack, J. B., Grinspoon, D. H., En-
crenaz, T., ... Taylor, F. W. (1993, Jul). Variations in Venus cloud particle
properties: a new view of Venus's cloud morphology as observed by the Galileo
near-infrared mapping spectrometer. *Planetary and Space Science*, *41*(7),
477-485. doi: 10.1016/0032-0633(93)90030-6
- Counselman, C. C., Gourevitch, S. A., King, R. W., Lorient, G. B., & Ginsberg, E. S.
(1980, December). Zonal and meridional circulation of the lower atmosphere
of Venus determined by radio interferometry. *Journal of Geophysical Research*,
85, 8026-8030.
- Crisp, D., McMurdock, S., Stephens, S. K., Sinton, W. M., Ragent, B., Hodapp,
K.-W., ... Elias, J. (1991, September). Ground-based near-infrared imaging
observations of Venus during the Galileo encounter. *Science*, *253*, 1538-1541.
- Drossart, P., Piccioni, G., Adriani, A., Angrilli, F., Arnold, G., Baines, K. H., ...
Afanasenko, T. Z. (2007, October). Scientific goals for the observation of
Venus by VIRTIS on ESA/Venus express mission. *Planetary and Space Sci-
ence*, *55*, 1653-1672. doi: 10.1016/j.pss.2007.01.003
- Fedorov, A. V., & Melville, W. K. (2000, Jan). Kelvin Fronts on the Equatorial
Thermocline. *Journal of Physical Oceanography*, *30*(7), 1692. doi: 10.1175/
1520-0485(2000)030<1692:KFOTET>2.0.CO;2
- Fukuhara, T., Futaguchi, M., Hashimoto, G. L., Horinouchi, T., Imamura, T.,
Iwagami, N., ... Yamazaki, A. (2017, January). Large stationary gravi-
ty wave in the atmosphere of Venus. *Nature Geoscience*, *10*, 85-88. doi:
10.1038/ngeo2873
- Garate-Lopez, I., & Lebonnois, S. (2018, Nov). Latitudinal variation of clouds'
structure responsible for Venus' cold collar. *Icarus*, *314*, 1-11. doi: 10.1016/j.
.icarus.2018.05.011
- Haghi, K. R., Parsons, D. B., & Shapiro, A. (2017, October). Bores Observed
during IHOP_2002: The Relationship of Bores to the Nocturnal Envi-
ronment. *Monthly Weather Review*, *145*(10), 3929-3946. doi: 10.1175/
MWR-D-16-0415.1
- Hinson, D. P., & Jenkins, J. M. (1995, April). Magellan radio occultation measure-
ments of atmospheric waves on Venus. *Icarus*, *114*, 310-327. doi: 10.1006/icar
.1995.1064
- Horinouchi, T., Murakami, S., Satoh, T., Peralta, J., Ogohara, K., Kouyama, T., ...
Young, E. F. (2017, September). Equatorial jet in the lower to middle cloud
layer of Venus revealed by Akatsuki. *Nature Geoscience*, *10*, 646-651. doi:
10.1038/ngeo3016
- Imai, M., Kouyama, T., Takahashi, Y., Yamazaki, A., Watanabe, S., Yamada, M.,

- 376 ... Horinouchi, T. (2019). Planetary-Scale Variations in Winds and UV
 377 Brightness at the Venusian Cloud Top: Periodicity and Temporal Evolution.
 378 *Journal of Geophysical Research: Planets*, *124*(10), 2635-2659. Retrieved
 379 from [https://agupubs.onlinelibrary.wiley.com/doi/abs/10.1029/](https://agupubs.onlinelibrary.wiley.com/doi/abs/10.1029/2019JE006065)
 380 [2019JE006065](https://agupubs.onlinelibrary.wiley.com/doi/abs/10.1029/2019JE006065) doi: 10.1029/2019JE006065
- 381 Imamura, T., & Hashimoto, G. L. (2001, Dec). Microphysics of Venusian Clouds in
 382 Rising Tropical Air. *Journal of Atmospheric Sciences*, *58*(23), 3597-3612. doi:
 383 [10.1175/1520-0469\(2001\)058<3597:MOVCIR>2.0.CO;2](https://doi.org/10.1175/1520-0469(2001)058<3597:MOVCIR>2.0.CO;2)
- 384 Imamura, T., Higuchi, T., Maejima, Y., Takagi, M., Sugimoto, N., Ikeda, K., &
 385 Ando, H. (2014, January). Inverse insolation dependence of Venus' cloud-level
 386 convection. *Icarus*, *228*, 181-188. doi: 10.1016/j.icarus.2013.10.012
- 387 Iwagami, N., Sakanoi, T., Hashimoto, G. L., Sawai, K., Ohtsuki, S., Takagi, S., ...
 388 Kouyama, T. (2018, January). Initial products of Akatsuki 1- μm camera.
 389 *Earth, Planets, and Space*, *70*, 6. doi: 10.1186/s40623-017-0773-5
- 390 Kouyama, T., Taguchi, M., Fukuhara, T., Imamura, T., Horinouchi, T., Sato, T. M.,
 391 ... Nakamura, M. (2019, Aug). Global Structure of Thermal Tides in the
 392 Upper Cloud Layer of Venus Revealed by LIR on Board Akatsuki. *Geophysical*
 393 *Research Letters*, *46*(16), 9457-9465. doi: 10.1029/2019GL083820
- 394 Lebonnois, S., Hourdin, F., Eymet, V., Cresspin, A., Fournier, R., & Forget, F.
 395 (2010, June). Superrotation of Venus' atmosphere analyzed with a full general
 396 circulation model. *Journal of Geophysical Research (Planets)*, *115*, E06006.
 397 doi: 10.1029/2009JE003458
- 398 Lebonnois, S., Sugimoto, N., & Gilli, G. (2016). Wave analysis in the atmosphere
 399 of Venus below 100-km altitude, simulated by the LMD Venus GCM. *Icarus*,
 400 *278*, 38–51. Retrieved from [http://www.sciencedirect.com/science/](http://www.sciencedirect.com/science/article/pii/S0019103516302688)
 401 [article/pii/S0019103516302688](http://www.sciencedirect.com/science/article/pii/S0019103516302688) doi: 10.1016/j.icarus.2016.06.004
- 402 Lefevre, M., Lebonnois, S., & Spiga, A. (2018, October). ThreeDimensional Tur-
 403 bulenceResolving Modeling of the Venusian Cloud Layer and Induced Gravity
 404 Waves: Inclusion of Complete Radiative Transfer and Wind Shear. *Journal of*
 405 *Geophysical Research (Planets)*, *123*(10), 2773-2789. Retrieved from [https://](https://agupubs.onlinelibrary.wiley.com/doi/full/10.1029/2018JE005679)
 406 agupubs.onlinelibrary.wiley.com/doi/full/10.1029/2018JE005679 doi:
 407 [10.1029/2018JE005679](https://doi.org/10.1029/2018JE005679)
- 408 Limaye, S. S., Watanabe, S., Yamazaki, A., Yamada, M., Satoh, T., Sato, T. M., ...
 409 Ocampo, A. C. (2018, January). Venus looks different at different wavelengths:
 410 morphology from Akatsuki multispectral images. *Earth, Planets, and Space*,
 411 *70*, 38. Retrieved from [https://link.springer.com/article/10.1186/](https://link.springer.com/article/10.1186/s40623-018-0789-5)
 412 [s40623-018-0789-5](https://link.springer.com/article/10.1186/s40623-018-0789-5) doi: 10.1186/s40623-018-0789-5
- 413 Magdalena, R. S. M., Scot, C. R. R., & Timothy, I. M. (2006). Numerical simulation
 414 of atmospheric bore waves on Mars. *Icarus*, *185*(2), 383-394. Retrieved from
 415 <http://www.sciencedirect.com/science/article/pii/S0019103506002375>
 416 doi: 10.1016/j.icarus.2006.07.006
- 417 McGouldrick, K., Momary, T. W., Baines, K. H., & Grinspoon, D. H. (2012, Febru-
 418 ary). Quantification of middle and lower cloud variability and mesoscale
 419 dynamics from Venus Express/VIRTIS observations at 1.74 μm . *Icarus*, *217*,
 420 615-628. doi: 10.1016/j.icarus.2011.07.009
- 421 Nakamura, M., Imamura, T., Ishii, N., Abe, T., Kawakatsu, Y., Hirose, C., ...
 422 Kamata, Y. (2016). AKATSUKI returns to Venus. *Earth, Planets*
 423 *and Space*, *68*(1), 1-10. Retrieved from [http://dx.doi.org/10.1186/](http://dx.doi.org/10.1186/s40623-016-0457-6)
 424 [s40623-016-0457-6](http://dx.doi.org/10.1186/s40623-016-0457-6) doi: 10.1186/s40623-016-0457-6
- 425 Navarro, T., Schubert, G., & Lebonnois, S. (2018, Jun). Atmospheric mountain wave
 426 generation on Venus and its influence on the solid planet's rotation rate. *Nature*
 427 *Geoscience*, *11*(7), 487-491. doi: 10.1038/s41561-018-0157-x
- 428 Ogohara, K., Takagi, M., Murakami, S.-y., Horinouchi, T., Yamada, M., Kouyama,
 429 T., ... Abe, T. (2017, December). Overview of Akatsuki data products: def-
 430 inition of data levels, method and accuracy of geometric correction. *Earth,*

- 431 *Planets, and Space*, 69, 167. doi: 10.1186/s40623-017-0749-5
- 432 Peralta, J., Hueso, R., Sánchez-Lavega, A., Lee, Y. J., Muñoz, A. G., Kouyama,
- 433 T., ... Satoh, T. (2017, August). Stationary waves and slowly moving fea-
- 434 tures in the night upper clouds of Venus. *Nature Astronomy*, 1, 0187. doi:
- 435 10.1038/s41550-017-0187
- 436 Peralta, J., Hueso, R., Sánchez-Lavega, A., Piccioni, G., Lanciano, O., & Drossart,
- 437 P. (2008, December). Characterization of mesoscale gravity waves in the upper
- 438 and lower clouds of Venus from VEX-VIRTIS images. *Journal of Geophysical*
- 439 *Research*, 113, E00B18+. doi: 10.1029/2008JE003185
- 440 Peralta, J., Iwagami, N., Sánchez-Lavega, A., Lee, Y. J., Hueso, R., Narita, M., ...
- 441 Takagi, S. (2019, Mar). Morphology and Dynamics of Venus's Middle Clouds
- 442 With Akatsuki/IR1. *Geophysical Research Letters*, 46(5), 2399-2407. doi:
- 443 10.1029/2018GL081670
- 444 Peralta, J., Muto, K., Hueso, R., Horinouchi, T., Sánchez-Lavega, A., Murakami,
- 445 S.-y., ... Luz, D. (2018, dec). Nightside Winds at the Lower Clouds of Venus
- 446 with Akatsuki/IR2: Longitudinal, local time and decadal variations from com-
- 447 parison with previous measurements. *The Astrophysical Journal Supplement*
- 448 *Series*, 239(29), 17. Retrieved from [http://iopscience.iop.org/article/](http://iopscience.iop.org/article/10.3847/1538-4365/aae844/meta)
- 449 [10.3847/1538-4365/aae844](http://iopscience.iop.org/article/10.3847/1538-4365/aae844/meta) doi: 10.3847/1538-4365/aae844
- 450 Peralta, J., Sánchez-Lavega, A., Horinouchi, T., McGouldrick, K., Garate-Lopez,
- 451 I., Young, E. F., ... Limaye, S. S. (2019, Nov). New cloud morphologies
- 452 discovered on the Venus's night during Akatsuki. *Icarus*, 333, 177-182. doi:
- 453 10.1016/j.icarus.2019.05.026
- 454 Peralta, J., Sánchez-Lavega, A., López-Valverde, M. A., Luz, D., & Machado, P.
- 455 (2015). Venus's major cloud feature as an equatorially trapped wave dis-
- 456 torted by the wind. *Geophysical Research Letters*, 42(3), 705-711. Retrieved
- 457 from <http://dx.doi.org/10.1002/2014GL062280> (2014GL062280) doi:
- 458 10.1002/2014GL062280
- 459 Rayner, J., Bond, T., Bonnet, M., Jaffe, D., Muller, G., & Tokunaga, A. (2012).
- 460 iSHELL: a 1-5 micron cross-dispersed R=70,000 immersion grating spec-
- 461 trograph for IRTF. In I. S. McLean, S. K. Ramsay, & H. Takami (Eds.),
- 462 *Ground-based and airborne instrumentation for astronomy iv* (Vol. 8446,
- 463 p. 832-843). SPIE. Retrieved from <https://doi.org/10.1117/12.925511>
- 464 doi: 10.1117/12.925511
- 465 Rayner, J. T., Toomey, D. W., Onaka, P. M., Denault, A. J., Stahlberger, W. E.,
- 466 Vacca, W. D., ... Wang, S. (2003, March). SpeX: a Medium-Resolution 0.8-
- 467 5.5 Micron Spectrograph and Imager for the NASA Infrared Telescope Facility.
- 468 *The Publications of the Astronomical Society of the Pacific*, 115, 362-382. doi:
- 469 10.1086/367745
- 470 Sánchez-Lavega, A., Lebonnois, S., Imamura, T., Read, P., & Luz, D. (2017, Novem-
- 471 ber). The Atmospheric Dynamics of Venus. *Space Science Reviews*, 212, 1541-
- 472 1616. doi: 10.1007/s11214-017-0389-x
- 473 Sánchez-Lavega, A., Peralta, J., Gomez-Forrellad, J. M., Hueso, R., Pérez-Hoyos,
- 474 S., Mendikoa, I., ... Watanabe, S. (2016, December). Venus Cloud Mor-
- 475 phology and Motions from Ground-based Images at the Time of the Akat-
- 476 suki Orbit Insertion. *The Astrophysical Journal Letters*, 833, L7. doi:
- 477 10.3847/2041-8205/833/1/L7
- 478 Satoh, T., Sato, T. M., Nakamura, M., Kasaba, Y., Ueno, M., Suzuki, M., ...
- 479 Ohtsuki, S. (2017, November). Performance of Akatsuki/IR2 in Venus
- 480 orbit: the first year. *Earth, Planets, and Space*, 69, 154. doi: 10.1186/
- 481 s40623-017-0736-x
- 482 Scarica, P., Garate-Lopez, I., Lebonnois, S., Piccioni, G., Grassi, D., Migliorini,
- 483 A., & Tellmann, S. (2019, Sep). Validation of the IPSL Venus GCM Ther-
- 484 mal Structure with Venus Express Data. *Atmosphere*, 10(10), 584. doi:
- 485 10.3390/atmos10100584

- 486 Sihto, S. L., Vuollekoski, H., Leppä, J., Riipinen, I., Kerminen, V. M., Korhonen, H.,
487 ... Kulmala, M. (2009, May). Aerosol dynamics simulations on the connection
488 of sulphuric acid and new particle formation. *Atmospheric Chemistry &
489 Physics*, 9(9), 2933-2947.
- 490 Tellmann, S., Pätzold, M., Häusler, B., Bird, M. K., & Tyler, G. L. (2009, April).
491 Structure of the Venus neutral atmosphere as observed by the Radio Science
492 experiment VeRa on Venus Express. *Journal of Geophysical Research (Planets)*,
493 114, E00B36. doi: 10.1029/2008JE003204
- 494 Titov, D. V., Ignatiev, N. I., McGouldrick, K., Wilquet, V., & Wilson, C. F. (2018,
495 Dec). Clouds and Hazes of Venus. *Space Science Reviews*, 214(8), 126. doi:
496 10.1007/s11214-018-0552-z
- 497 Wilson, C. F., Guerlet, S., Irwin, P. G. J., Tsang, C. C. C., Taylor, F. W., Carlson,
498 R. W., ... Piccioni, G. (2008, November). Evidence for anomalous cloud particles
499 at the poles of Venus. *Journal of Geophysical Research (Planets)*, 113,
500 E00B13. doi: 10.1029/2008JE003108
- 501 Yakovlev, O. I., Matyugov, S. S., & Gubenko, V. N. (1991). Venera-15 and
502 -16 middle atmosphere profiles from radio occultations: Polar and near-
503 polar atmosphere of Venus. *Icarus*, 94(2), 493-510. Retrieved from
504 <http://www.sciencedirect.com/science/article/pii/001910359190243M>
505 doi: 10.1016/0019-1035(91)90243-M
- 506 Yamamoto, M., & Tanaka, H. (1997, June). Formation and Maintenance of the
507 4-Day Circulation in the Venus Middle Atmosphere. *Journal of Atmospheric
508 Sciences*, 54, 1472-1489. doi: 10.1175/1520-0469(1997)054<1472:FAMOTD>2.0
509 .CO;2
- 510 Yamazaki, A., Yamada, M., Lee, Y. J., Watanabe, S., Horinouchi, T., Murakami,
511 S., ... Nakamura, M. (2018, February 12). Ultraviolet imager on Venus
512 orbiter Akatsuki and its initial results. *Earth, Planets and Space*, 70(1),
513 23. Retrieved from <https://doi.org/10.1186/s40623-017-0772-6> doi:
514 10.1186/s40623-017-0772-6

Figure 1.

Author Manuscript

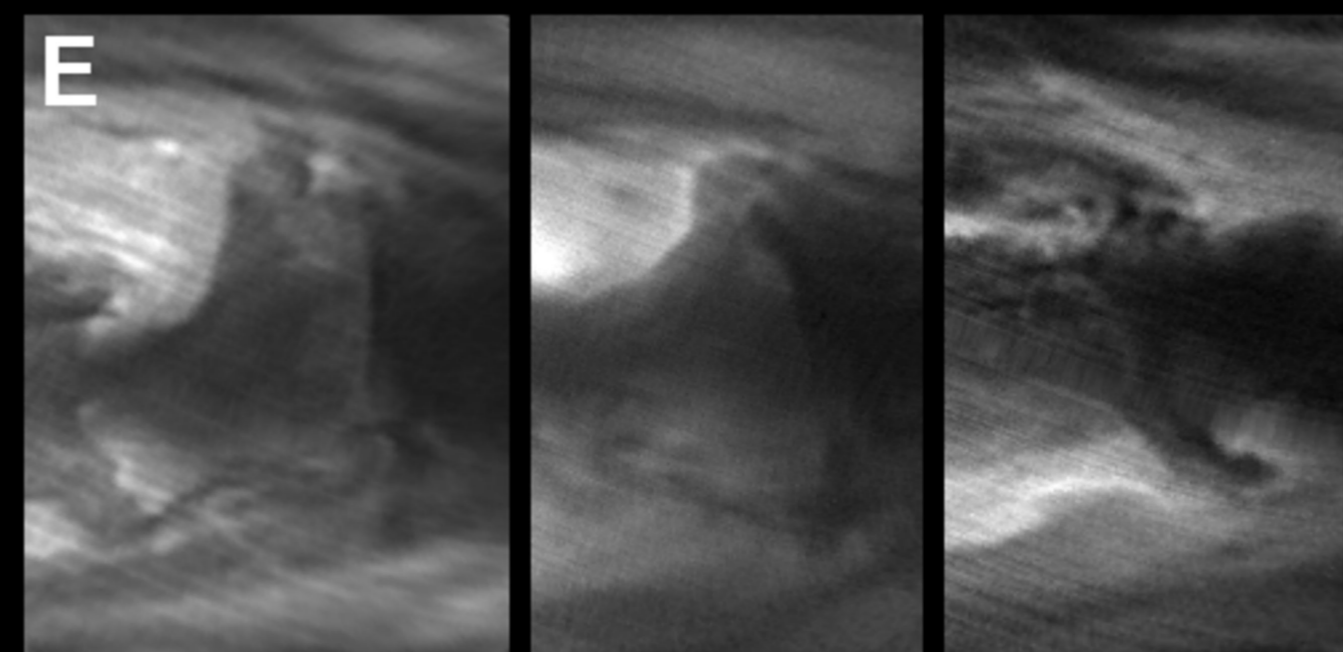
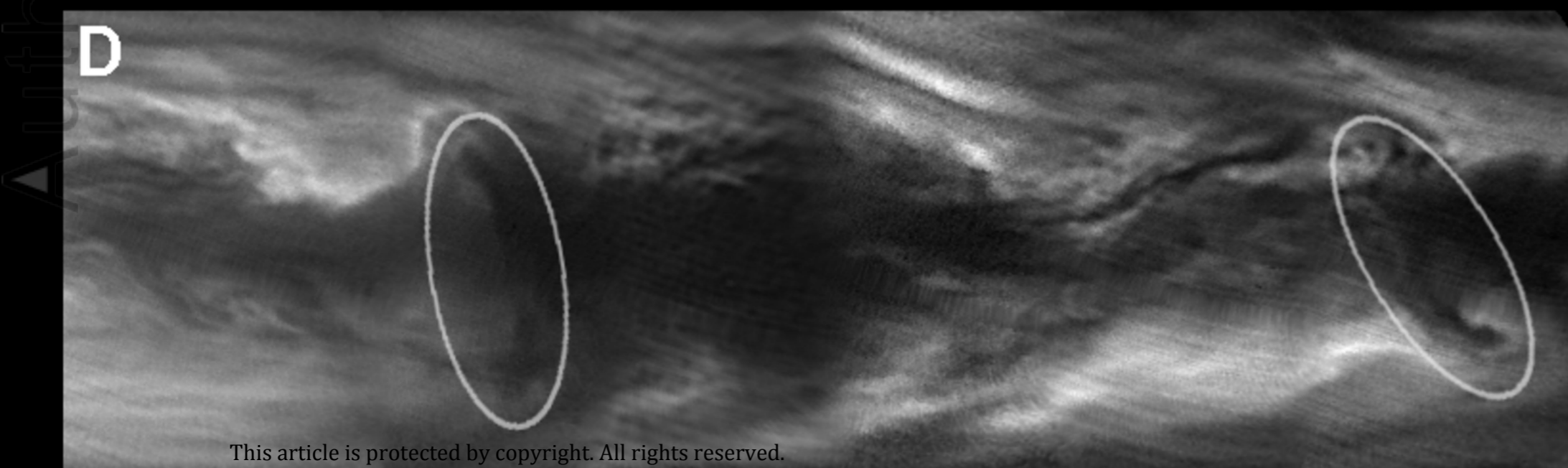
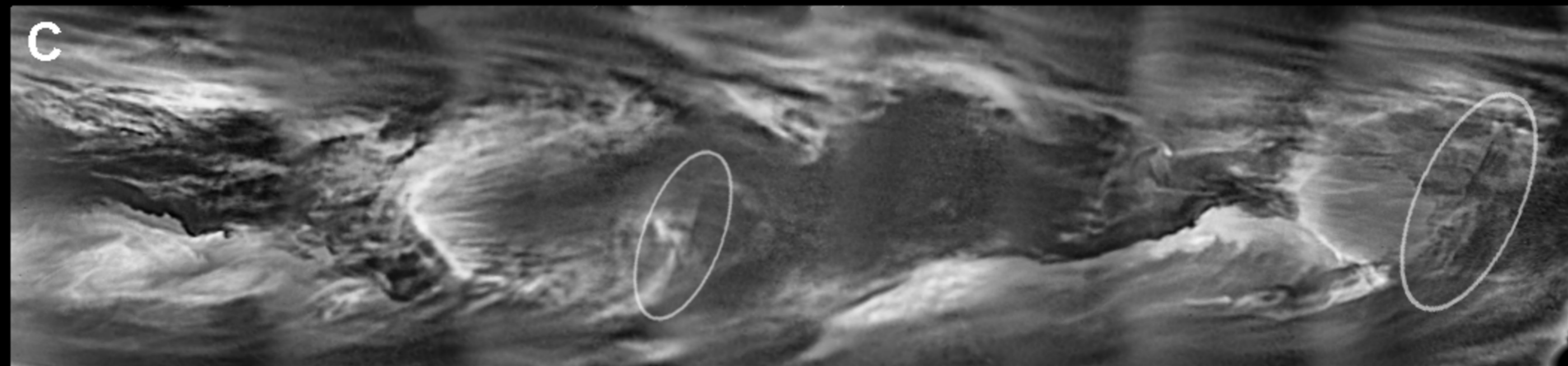
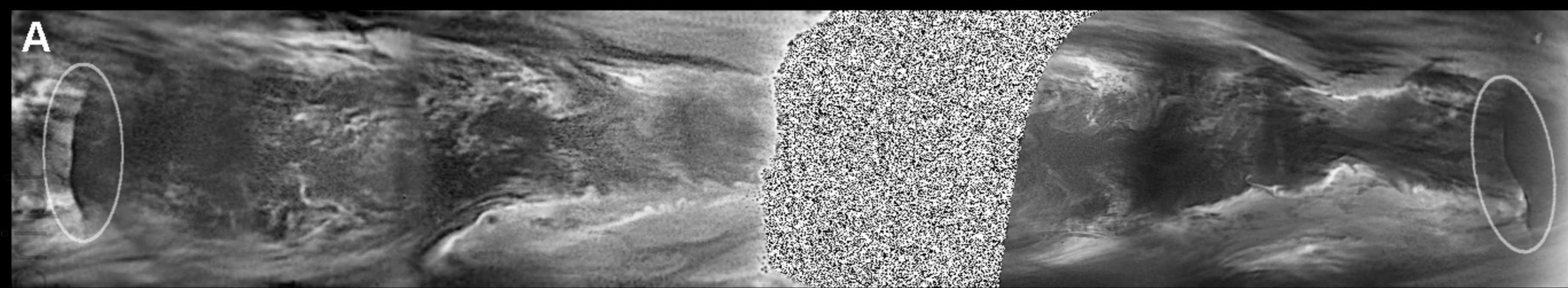


Figure 2.

Author Manuscript

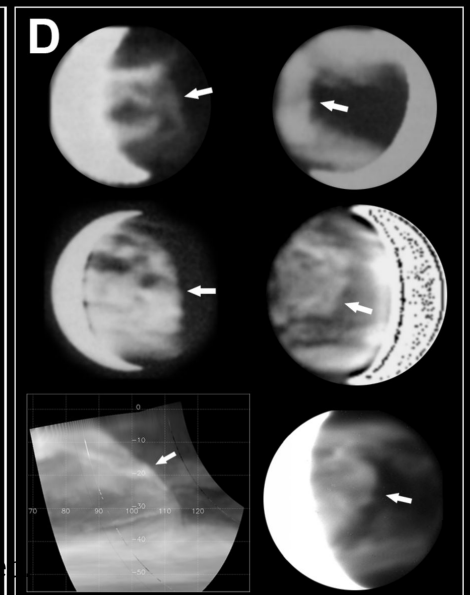
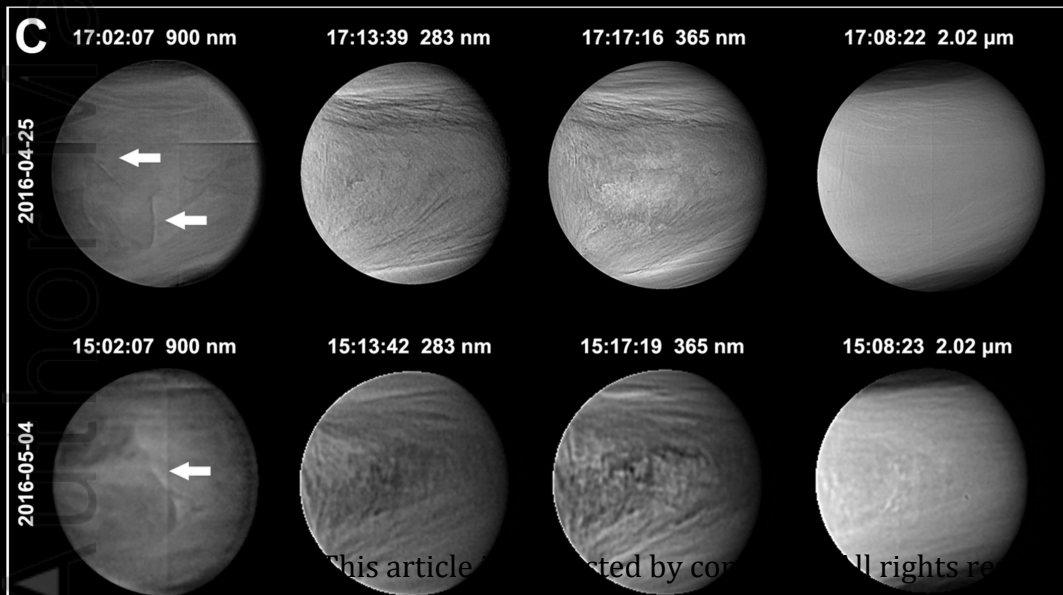
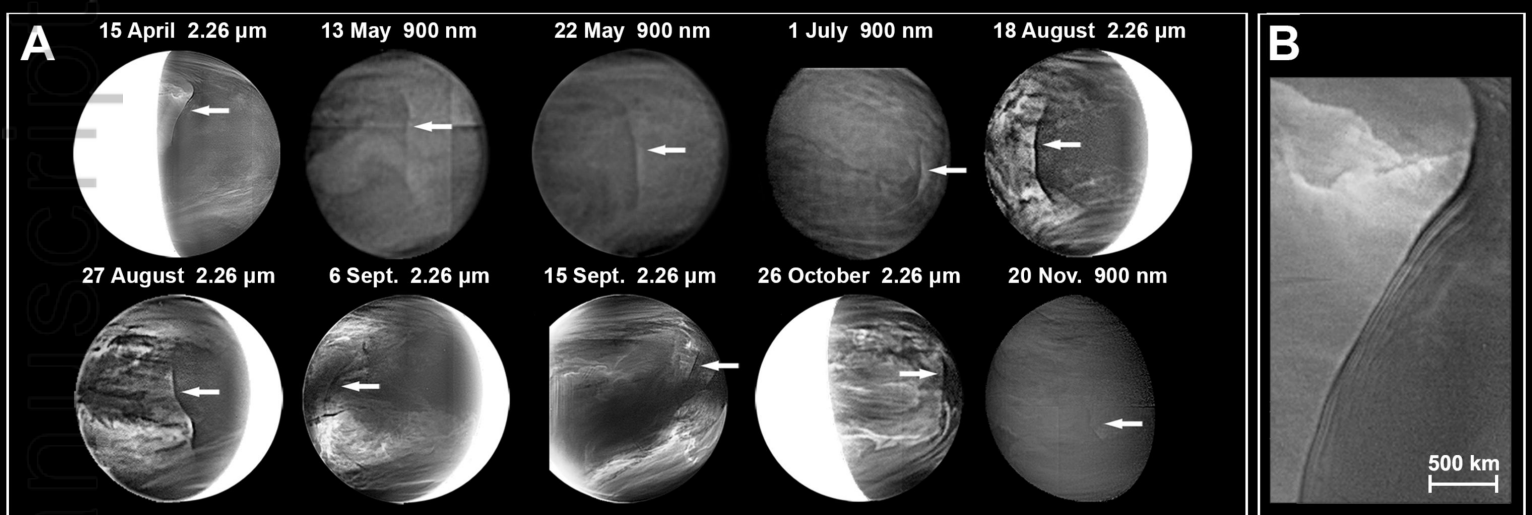


Figure 3.

Author Manuscript

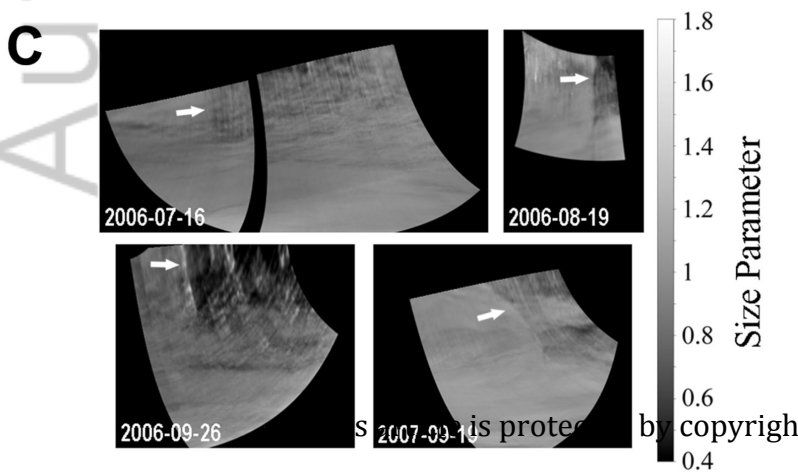
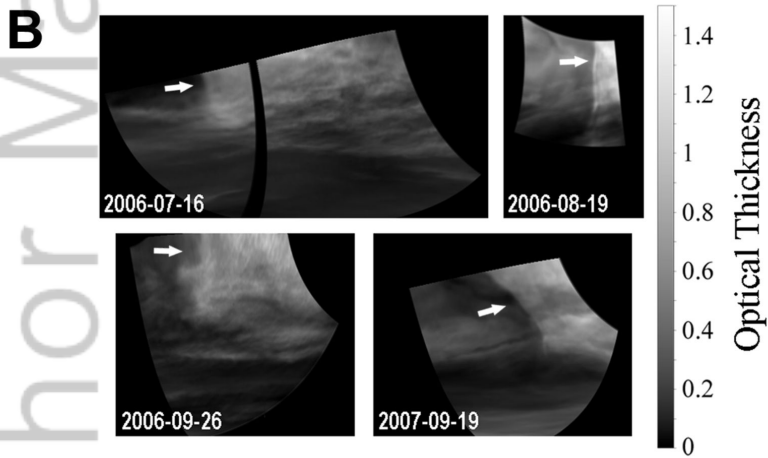
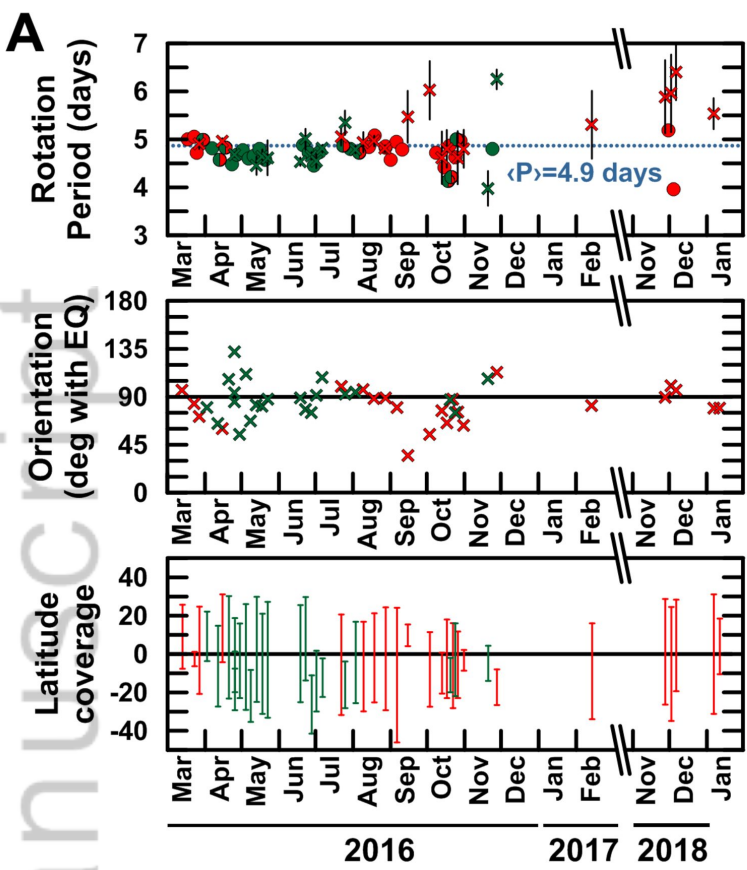
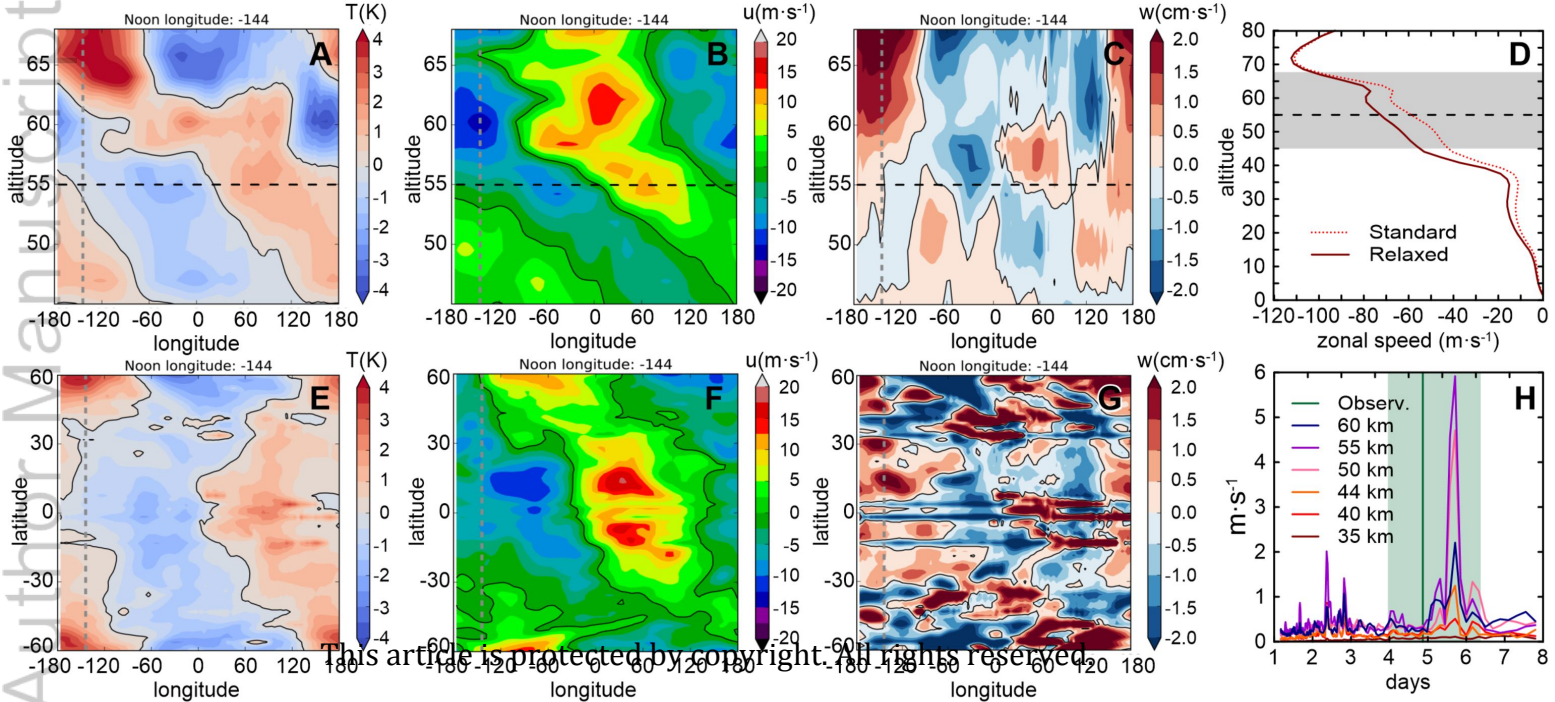
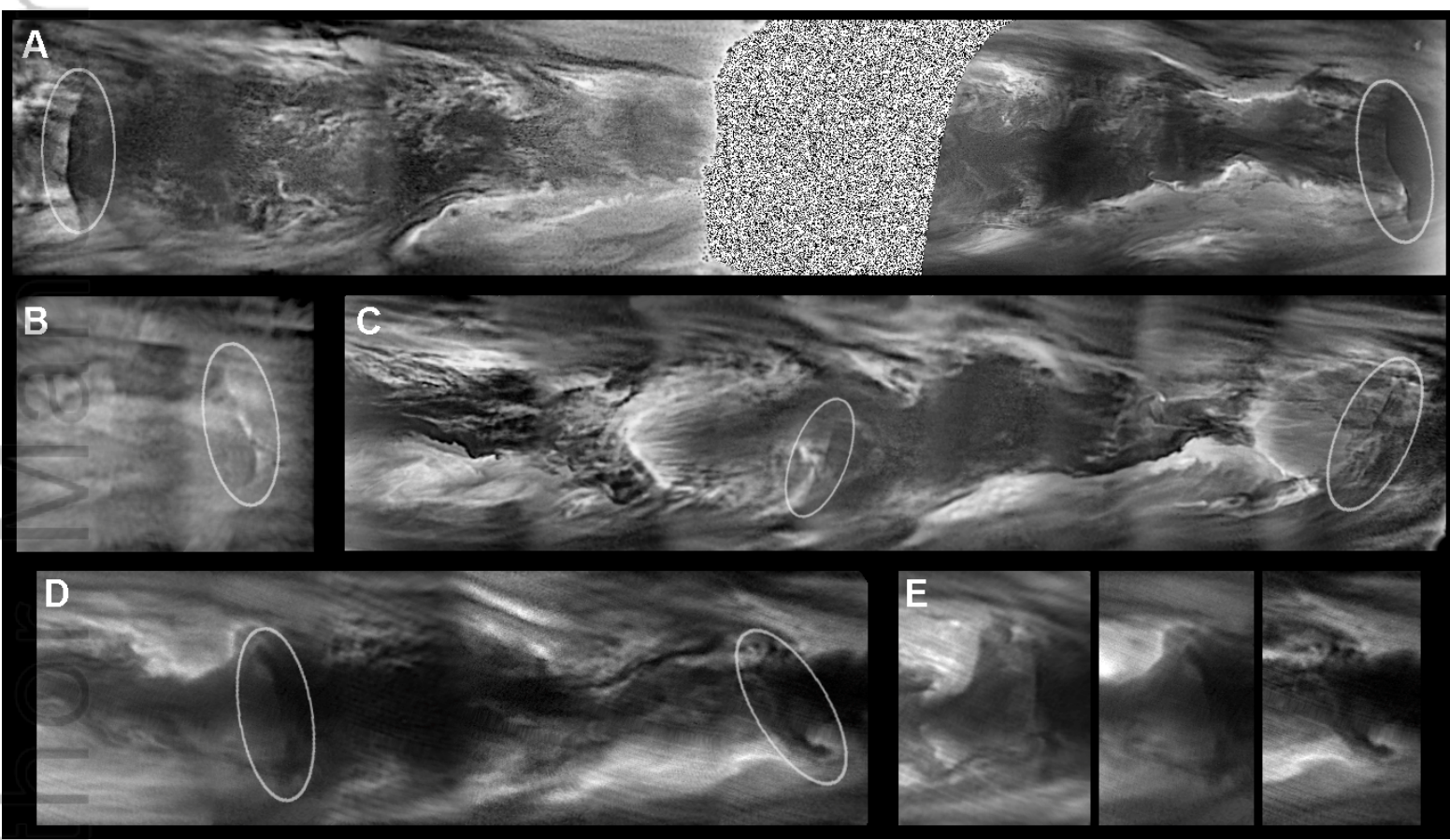


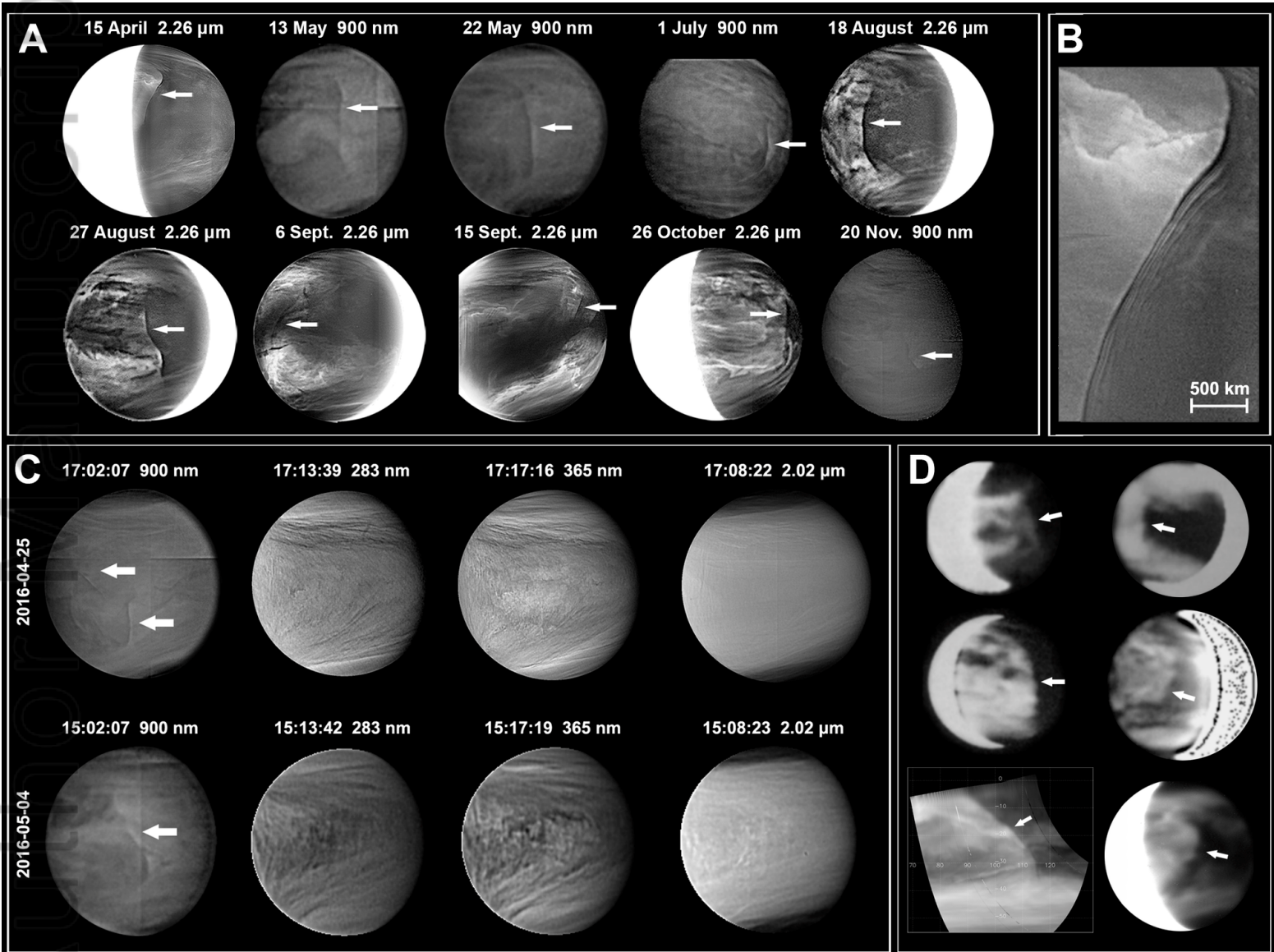
Figure 4.

Author Manuscript

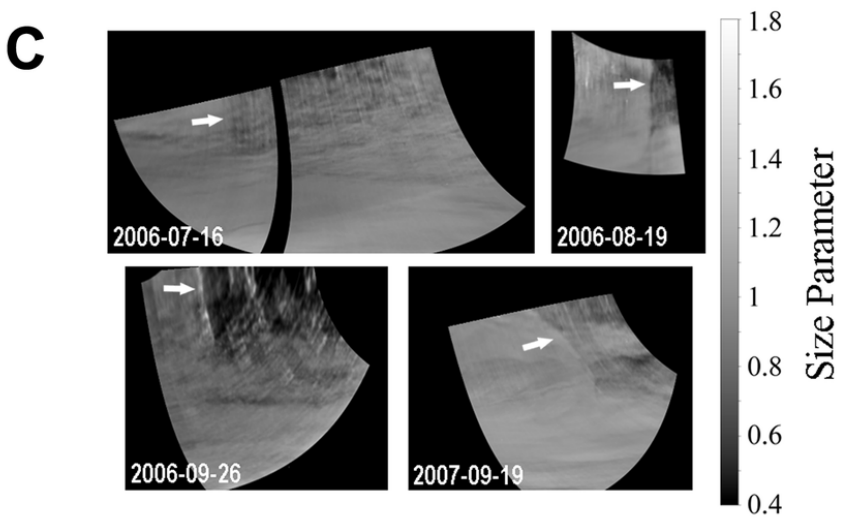
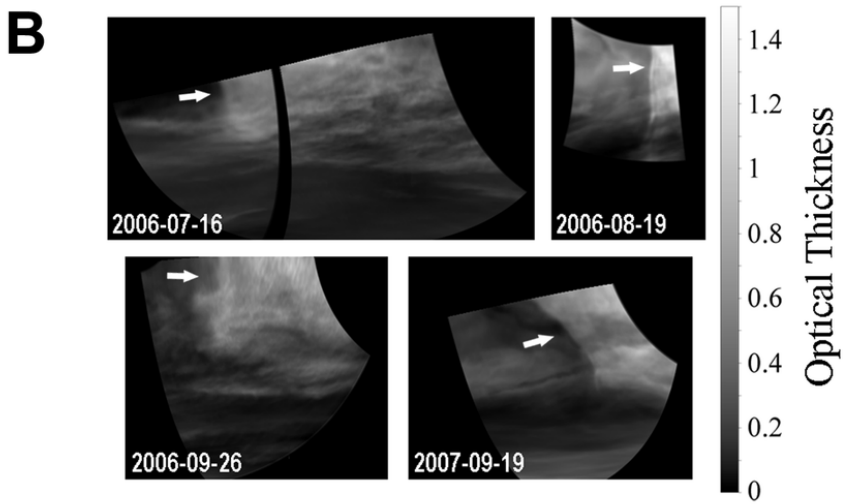
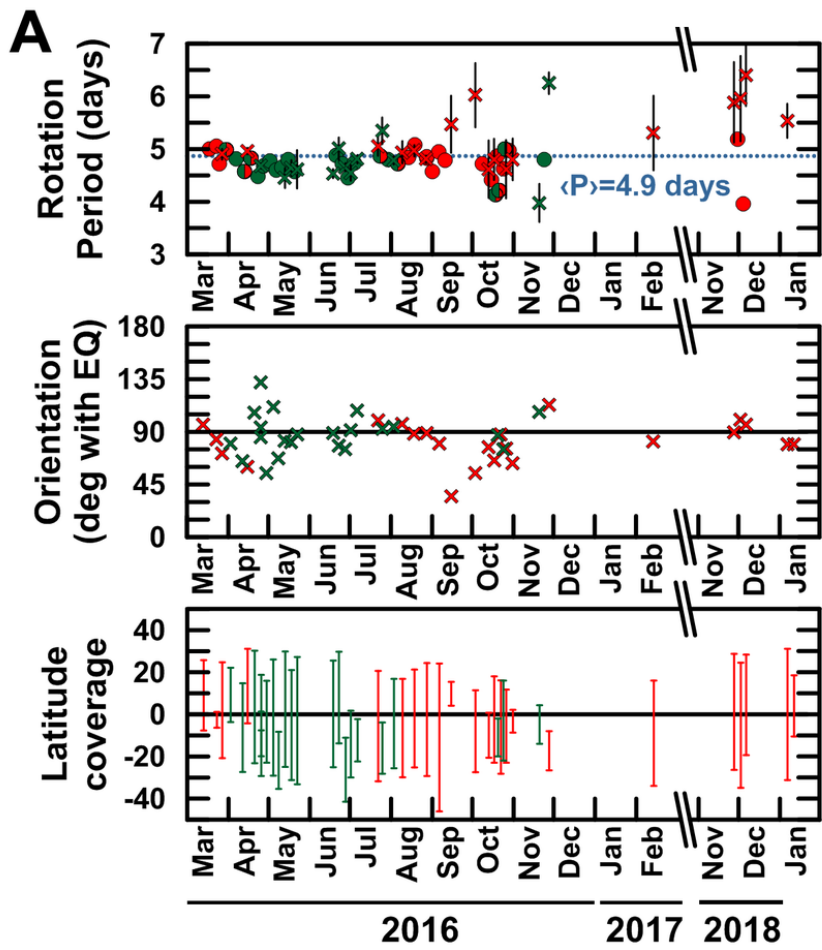




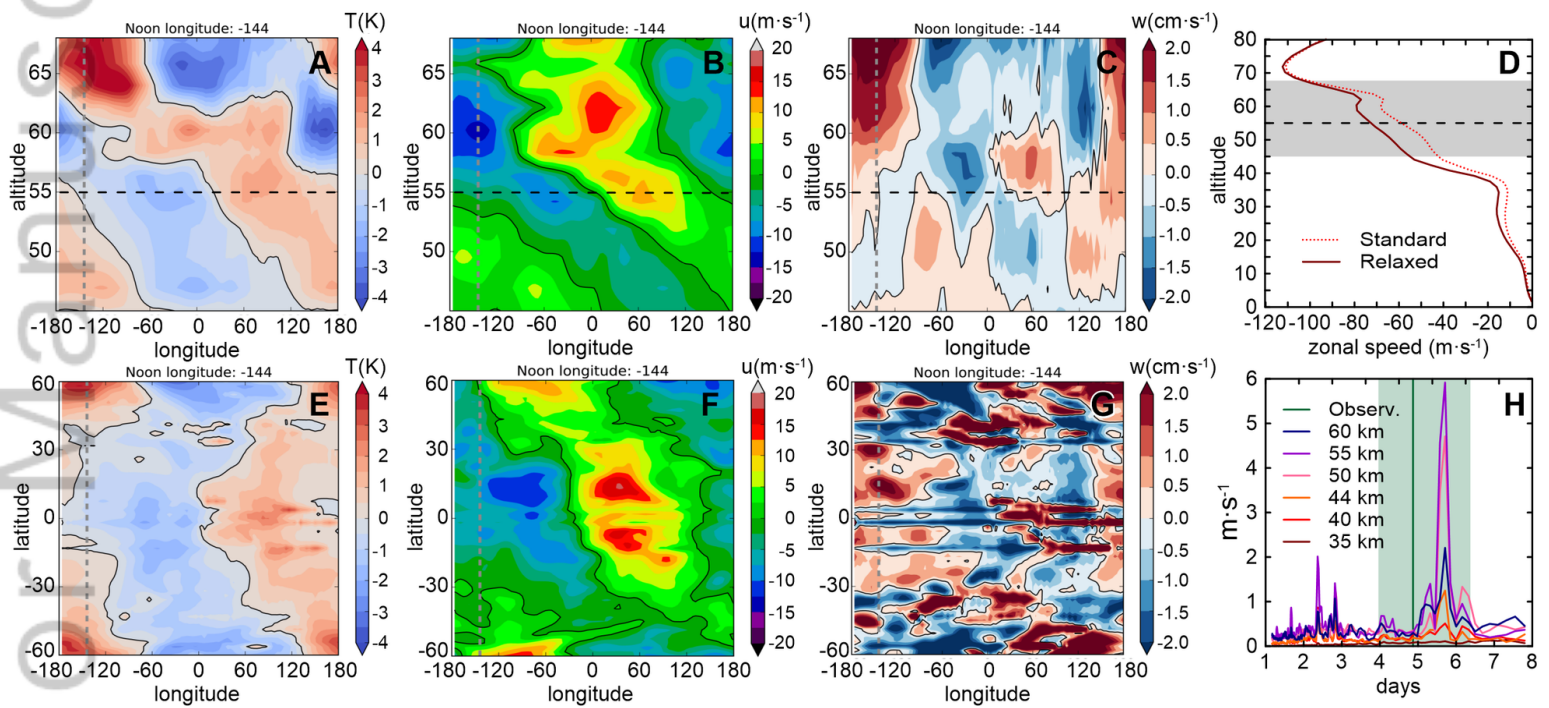
2020GL087221-f01-z-.png



2020GL087221-f02-z-.png



2020GL087221-f03-z.png



2020GL087221-f04-z-.png